PROSPECTS
IN PHARMACEUTICAL SCIENCES

Prospects in Pharmaceutical Sciences, 24(3), 1-17
https://prospects.wum.edu.pl/

Original Article

PRONIOSOMAL ENCAPSULATION OF TENOFOVIR FOR IMPROVED STABILITY AND CONTROLLED RELEASE: A FACTORIAL DESIGN-BASED STUDY

Swarupa Arvapalli[1], Anka Rao Areti[1]*

[1] [1]Department of Pharmaceutics, KL College of Pharmacy, Koneru Lakshmaiah Education Foundation, Vaddeswaram, Andhra Pradesh, India-522022.

* Correspondence, e-mail: drankarao83@gmail.com

Received: 28.05.2025 / Revised: 24.08.2025 /Accepted: 23.09.2025 / Published: 17.07.2026

ABSTRACT

Tenofovir, a widely used antiviral agent, suffers from poor stability, low bioavailability, and rapid renal clearance, limiting its therapeutic efficacy. Proniosomes, a vesicular drug delivery system, offer a promising approach to enhance tenofovir's stability and controlled release. A factorial design approach was employed to optimize tenofovir-loaded proniosomes, evaluating key formulation variables such as surfactant type, cholesterol concentration, and maltodextrin concentration. The formulations were evaluated for particle size, polydispersity index (PDI), zeta potential, and encapsulation efficiency (EE%), with morphological characteristics examined through SEM and TEM imaging. In vitro, drug release studies were conducted to assess the controlled release behavior, while stability studies evaluated the formulation's robustness under different storage conditions. The optimized formulation showed a particle size of around 420 nm, a low PDI (< 0.3), a zeta potential of -28.6 mV, and an encapsulation efficiency of 87.3%, reflecting its stability and uniform vesicle distribution. The in vitro release profile showed prolonged drug release over 24 hours, beginning with an initial burst phase followed by a controlled diffusion phase. The release kinetics followed the Korsmeyer-Peppas model, suggesting a non-Fickian diffusion mechanism. Stability studies showed minimal changes in physicochemical properties over three months, confirming formulation stability. The study highlights proniosomes as an effective delivery system for tenofovir, offering enhanced stability, sustained release, and improved encapsulation efficiency. This approach presents a potential alternative for improving the pharmacokinetic profile of tenofovir, ensuring better therapeutic outcomes in antiviral therapy.

KEYWORDS: tenofovir, proniosomes, controlled release, factorial design, encapsulation efficiency.

1. Introduction

Tenofovir, a nucleotide reverse transcriptase inhibitor (NRTI), is widely utilized for the treatment and prevention of HIV/AIDS and hepatitis B infections. It is a key component of combination antiretroviral therapy (cART) due to its potent antiviral activity, long intracellular half-life, and high genetic barrier to resistance [1, 2]. Despite its clinical effectiveness, tenofovir presents several formulation and pharmacokinetic challenges that limit its therapeutic potential. Its poor oral bioavailability (~25%) is primarily due to high hydrophilicity and low permeability (BCS Class III drug), restricting passive diffusion across biological membranes and leading to suboptimal systemic absorption [3–5]. Additionally, tenofovir has a short plasma half-life (~17 hours) due to rapid renal clearance, necessitating once-daily dosing. Prolonged high systemic drug levels can contribute to renal toxicity, particularly through its active transport by organic anion transporters (OAT1 and OAT3) in the kidneys, leading to drug accumulation in proximal tubular cells [6–8]. This is further associated with bone mineral density loss, likely due to phosphate imbalance. Another major drawback is chemical instability, as tenofovir is prone to degradation and hydrolysis, which affects its shelf-life and overall therapeutic efficiency [9]. The aqueous instability of its prodrug, tenofovir disoproxil fumarate (TDF), necessitates stabilization strategies to maintain efficacy. Moreover, tenofovir's poor tissue targeting limits its antiviral action, as effective therapy requires its intracellular conversion to tenofovir diphosphate [10, 11]. Conventional formulations fail to efficiently target infected tissues, resulting in suboptimal drug concentrations at the site of action. These challenges highlight the need for advanced drug delivery systems to enhance tenofovir's bioavailability, stability, and targeted delivery

while minimizing systemic toxicity [12].

Several delivery approaches have been explored to enhance the bioavailability and therapeutic efficacy of tenofovir (TFV), addressing its poor cell permeability, low oral bioavailability, and systemic toxicity. These include long-acting ProTide nanocrystals, which improve intracellular retention and extend drug release [13]; pH-sensitive hydrogels that provide controlled release in response to physiological conditions [14, 15]; and ω-functionalized lipid prodrugs designed to enhance hepatic stability and prolong circulation [16]. Other strategies involve buccal patches for rapid dissolution [17], vaginal tablets for sustained HIV prevention [18], and nanotechnology-based carriers such as polymeric nanoparticles and liposomes, each showing varied success in improving drug absorption and reducing systemic toxicity [19–22]. However, these approaches have limitations, including complex manufacturing processes, stability concerns, and variability in patient adherence.

Proniosomes offer a promising strategy to overcome the limitations associated with tenofovir delivery. These vesicular drug carriers enhance solubility, stability, bioavailability, and controlled release, making them ideal for tenofovir, which suffers from poor permeability, rapid renal clearance, and toxicity concerns. Proniosomes convert into niosomes upon hydration, providing a stable, biodegradable, and biocompatible system for drug encapsulation [23, 24]. Their lipophilic bilayer structure enables better membrane permeability, improving tenofovir's systemic absorption. Additionally, proniosomes protect tenofovir from hydrolysis, prolong circulation time, and reduce renal accumulation, potentially lowering nephrotoxicity. The ability of proniosomes to enhance intracellular uptake can also improve the conversion of tenofovir into its active diphosphate form, ensuring better antiviral activity at the target site [25–27]. Given these advantages, proniosomal encapsulation represents a viable nanocarrier-based approach for improving tenofovir delivery while minimizing adverse effects.

This study aims to establish proniosomes as a novel and effective nanocarrier system for tenofovir delivery, addressing challenges related to solubility, bioavailability, stability, and toxicity while ensuring enhanced therapeutic efficacy.

2. Materials and methods

Tenofovir was obtained from Aurobindo Pharma in Hyderabad, India. Maltodextrin, Span® 60, and cholesterol were sourced from Sigma-Aldrich Chemicals Private Limited, Bangalore, India. All other reagents and chemicals utilized in the experiments were of analytical grade and were used without further purification. Millipore water was used throughout all the experiments.

2.1. Optimization of Formulation Using Experimental Design and Optimization

A 24 full factorial design was implemented using Design-Expert® software (V13.0.5.0) to systematically evaluate the impact of critical process parameters (CPPs) on the key attributes of tenofovir-loaded proniosomes. Four independent variables were selected: Span 60 (A), cholesterol (B), drug (C), and maltodextrin (% w/v) (D), each studied at two levels. These factors were chosen for their potential to influence formulation stability and performance. The dependent variables, defined as critical quality attributes (CQAs), were particle size (Y1), polydispersity index (PDI) (Y2), and encapsulation efficiency (EE%) (Y3). The factorial design allowed for the assessment of both main effects and interactions among these factors. Optimization criteria focused on maximizing EE% for higher drug loading, minimizing PDI for uniform particle distribution, and achieving optimal nanosized particles for enhanced stability and bioavailability.

2.2. Preparation and Hydration of Maltodextrin-Coated Proniosomes to Form Niosomes

Proniosomes were prepared by dissolving Span 60, cholesterol, and tenofovir in ethanol, vortexing, and incubating at 70°C for 5 minutes. The solvent was evaporated under reduced pressure to form a lipid film, which was hydrated with deionized water at 60°C and sonicated for 15 minutes to yield a proniosomal powder.

For maltodextrin-coated proniosomes, the lipid film was treated with Sorensen's phosphate buffer (pH 7.4) containing 0.02% maltodextrin and evaporated at 60°C. Uncoated and blank proniosomes were prepared similarly, using a buffer without maltodextrin or omitting the drug, respectively.

To form niosomes, the proniosomal powder was hydrated with phosphate buffer (pH 6.8) at 40°C under gentle agitation. Hydration volumes (5–25 mL) and times (5–30 minutes) were optimized to achieve high encapsulation efficiency, uniform size distribution, and stable vesicle formation, suitable for drug delivery [28].

2.3. Characterization of Drug-Loaded Proniosomal Formulations

2.3.1. Determination of Entrapment Efficiency in Niosomes

Entrapment efficiency (EE%) was determined by dispersing reconstituted proniosomal powder in phosphate buffer (pH 6.8), followed by ultracentrifugation at 15,000 rpm for 30 minutes at 0°C to separate the free drug from the encapsulated drug. The supernatant, containing the unencapsulated drug, was removed, and the niosomal pellets were washed and resuspended to ensure complete separation. The supernatant was diluted to 10 mL and analyzed using UV-visible spectrophotometry to quantify the free drug concentration. EE% was calculated as the proportion of the total drug successfully encapsulated within the niosomal bilayers or aqueous compartments.

$$\text{Entrapment efficiency} = \frac{C_t - C_r}{C_t} X\ 100 \quad (1)$$

Where C_t is the concentration of the total amount of the drug and C_r is the concentration of the free drug.

2.3.2. Determination of Vesicle Size (PS), Polydispersity Index (PDI), and Zeta Potential (ZP)

Vesicle size (PS), polydispersity index (PDI), and zeta potential (ZP) of drug-loaded proniosomes were measured using Nanotrac Wave II (Malvern Instruments, UK) via dynamic light scattering (DLS). The niosomal dispersion was diluted appropriately to avoid interference, and measurements were conducted at room temperature

in triplicate for accuracy. PS was determined based on light scattering fluctuations, while PDI indicated size uniformity, with lower values reflecting a more homogeneous population. ZP assessed surface charge and colloidal stability, with higher absolute values reducing aggregation and enhancing system stability.

2.3.3. Microscopical and electron microscope examination

Vesicle formation in drug-loaded proniosomes was confirmed using optical microscopy, TEM, and SEM for detailed structural analysis. For optical microscopy, a niosome suspension was air-dried on a glass slide and observed at 100x magnification, with images captured digitally. SEM (HITACHI S-4100) analyzed the surface morphology of the proniosomal powder, with samples gold-coated for conductivity and imaged at 15 kV. For higher-resolution imaging, TEM was used. Niosomal dispersions were negatively stained with 1% uranyl acetate, deposited on a carbon-coated grid, and examined at 20,000x to 50,000x magnification, providing detailed insights into vesicle structure and surface characteristics.

2.3.4. In vitro Release Studies

The in vitro release kinetics of drug-loaded maltodextrin niosomes were studied in simulated intestinal fluid (SIF, pH 6.8) to mimic physiological conditions. Niosomal dispersions containing 5 mg of the drug were placed in dialysis bags (MWCO 12,000 g/mol, Sigma, USA) and immersed in 100 mL of SIF, stirred at 100 rpm. To maintain sink conditions, the medium was replaced after each sampling, and drug release was analyzed using HPLC for precise quantification.

To characterize drug release behavior, zero-order, first-order, Higuchi, and Korsmeyer-Peppas models were applied to cumulative release data. Zero-order kinetics indicates a constant release rate, while first-order kinetics suggests a release rate dependent on drug concentration. The Higuchi model describes diffusion-controlled release, and the Korsmeyer-Peppas model provides insight into the release mechanism, distinguishing between Fickian diffusion, anomalous transport, and erosion-based release. The release exponent (n) from the Korsmeyer-Peppas model further classifies the release mechanism, guiding formulation optimization for controlled and sustained drug delivery [29, 30].

2.3.5. Measurement of Angle of Repose

The angle of repose of dry proniosomes powder was measured using the funnel method to evaluate flow properties. The powder was poured through a 13 mm outlet positioned 10 cm above a flat surface, forming a conical pile. The angle of repose was calculated from the cone height and base diameter, providing essential insights into the flowability of the powder for processing and formulation.

2.3.6. Differential Scanning Calorimetric (DSC) and Fourier Transform Infrared (FTIR) Studies

FTIR spectroscopy was performed using a Bruker Optics FTIR spectrometer to analyze pure drugs, maltodextrin, their physical mixtures (1:0.005), and drug-loaded proniosomes. Spectra were recorded from 3500–500 cm^{-1} to identify characteristic peaks and potential interactions. Differential scanning calorimetry (DSC) was conducted using a Shimadzu DSC 2910, where powdered samples were heated at 10°C/min, and thermograms were analyzed for melting points, phase transitions, and drug-excipient interactions.

2.3.7. Quantitative Measurement of Intracellular Drug Content in NCI-N87 Gastric Cells Using HPLC Analysis

NCI-N87 gastric cells (2×10^5 cells/well) were seeded in 6-well plates and incubated overnight. The medium was then replaced with fresh DMEM containing free drug or maltodextrin niosomes (100 µg/mL drug concentration) and incubated at 37°C for 4 hours. After incubation, cells were washed twice with PBS, centrifuged (1000 rpm), and resuspended in PBS + 1× Triton X-100. The suspension was lysed using an ultrasonic water bath, and drug content was quantified via HPLC [31].

2.3.8. MDR1 Efflux Activity

MDR1 limits drug bioavailability by restricting cellular uptake. To assess MDR1 efflux, MDCK-MDR1 and Caco-2 cells (3×10^5 cells/well) were seeded in 12-well Transwell plates and incubated for 3 days to form confluent monolayers. TEER measurements confirmed monolayer integrity. Free TNF and TNF-coated proniosomes were added to the apical compartment with and without colchicine (MDR1 inhibitor). Colchicine and propranolol were used as controls. After 2 hours at 37°C, 160 rpm, samples from apical and basolateral compartments were analyzed by HPLC to determine A→B and B→A transport, assessing MDR1-mediated efflux [32].

2.3.9. Cytotoxicity Studies Using MTT Assay

The MTT assay was used to assess the cytotoxicity of drug-loaded proniosomes and free drugs in Caco-2 cells. Cells (1×10^4/well) were seeded in 96-well plates and cultured for 48 hours. Samples (0.1–200 µg/mL) were prepared in DMEM and incubated with cells at 37°C. After 4, 24, and 48 hours, the medium was replaced with an MTT reagent (1 mg/mL, 150 µL) and incubated for 4 hours. The formazan crystals were solubilized with DMSO (150 µL), and absorbance was measured at 590 nm using a Tecan plate reader. Cell viability was calculated relative to untreated controls.

2.3.10. Western Blot Analysis

To assess MDR1-mediated efflux, MDCK-MDR1 and Caco-2 cells (2×10^5/well) were seeded in 6-well plates and treated with TNF-coated proniosomes (10 µM) for 12 hours. Cells were lysed in an ice-cold buffer containing Tris, EDTA, Triton X-100, protease inhibitors, PMSF, and Na_3VO_4, then centrifuged at 13,000 g. SDS-PAGE was performed using 25 µg protein extract, followed by immunoblotting with anti-P-gp1/MDR1 antibody. Detection was done with peroxidase-conjugated secondary antibody and chemiluminescence, with anti-tubulin antibody used as a loading control.

2.3.11. Stability Studies

Comprehensive accelerated stability studies were conducted on the optimized tenofovir-loaded proniosomal formulation following ICH guidelines Q1A(R2) and Q1B to evaluate physical and chemical stability under five distinct storage conditions over 90 days: refrigerated

(4°C ± 2°C), room temperature (25°C ± 2°C/60% RH ± 5% RH), accelerated (40°C ± 2°C/75% RH ± 5% RH), photostability testing (25°C ± 2°C with 1.2 million lux hours and 200 watt hours/m² UV exposure using D65/ID65 fluorescent lamps), and high humidity stress (40°C ± 2°C/75% RH maintained using saturated sodium chloride solutions). Proniosomal formulations were dispensed into appropriate glass vials (amber for regular conditions, transparent for photostability) and stored in calibrated stability chambers (Thermolab Scientific Equipment Pvt. Ltd., Mumbai, India) with continuous environmental monitoring. Samples were withdrawn at predetermined intervals (0, 30, 60, and 90 days) and analyzed in triplicate for critical quality attributes including particle size distribution using dynamic light scattering (Malvern Zetasizer Nano ZS), drug content determination via validated HPLC methodology with samples dissolved in methanol and filtered through 0.45 µm membranes, and visual inspection for physical changes. Acceptance criteria were established as particle size increase < 10% from baseline, drug content retention ≥ 95%, and absence of significant visual changes, with statistical analysis performed using mean ± SD (n=3) to ensure reproducibility and regulatory compliance for shelf-life determination and storage recommendations.

2.3.12. In vivo Studies

2.3.12.1. Animals

Male Wistar rats (250 ± 20 g) were housed in propylene cages under controlled conditions (30°C, 60% RH), with ad libitum access to food and water. The animals underwent overnight fasting before the study. All procedures were approved by the Institutional Animal Ethics Committee (IAEC), PGP Life Science, Hyderabad (Approval No. PGP/AF/CP-00181/07/2022) and complied with CPCSEA guidelines.

2.3.12.2. In vivo pharmacokinetic studies

Four groups of male Wistar rats (n = 6 per group) were administered a single oral dose (10 mg/kg) to assess bioavailability. Group 1 received a pure drug suspension in 5% methylcellulose, while Group 2 received a marketed formulation. Groups 3 and 4 were given drug-loaded proniosomes, with Group 3 receiving TNF-coated proniosomes and Group 4 receiving non-coated proniosomes. All formulations were administered orally using a syringe and feeding tube.

Blood samples were collected via retro-orbital venous plexus puncture at 0.5, 1.5, 2, 2.5, 3, 3.5, 4, 4.5, 5, 8, 12, 24, 48, and 72 hours post-dose. Plasma was separated by centrifugation (3400 rpm, 15 min, 4°C) and stored at -20°C for analysis. For HPLC quantification, 200 µL acetonitrile was added to the plasma, vortexed (5 min), and centrifuged (5000 rpm, 15 min). The organic phase was evaporated under vacuum, and the residue was reconstituted in 0.15 mL mobile phase, vortexed (1 min), and centrifuged (13,000 rpm, 5 min). A 20 µL of supernatant was injected into an HPLC column for analysis.

3. Results and Discussion

A 2^4 full factorial design was employed to evaluate the effect of four critical process parameters (CPPs) – Span 60, cholesterol, tenofovir, and maltodextrin – on three critical quality attributes (CQAs): particle size (Y1), polydispersity index (PDI, Y2), and encapsulation efficiency (EE%, Y3) in tenofovir-loaded proniosomes. The goal was to achieve nano-sized particles (<200 nm), low PDI (≤0.3), and high EE% (≥70%).

Span 60 (A) is a long-chain, high–phase-transition non-ionic surfactant that forms tightly packed bilayers, lowering membrane permeability and increasing encapsulation efficiency while imparting good physical stability. Its hydrophobicity favors loading of poorly water-soluble drugs and typically yields lower PDI when optimized. Excess Span 60, however, can raise viscosity during film formation and increase particle size.

Cholesterol (B) inserts between surfactant chains to modulate bilayer rigidity and elasticity, reducing leakage and improving storage stability. An optimal cholesterol fraction minimizes permeability without over-stiffening the membrane. At very high levels, cholesterol can displace drug from the bilayer, lowering EE% and sometimes increasing vesicle size.

The drug load (C) governs the thermodynamic driving force for entrapment and influences bilayer packing. Within an optimal window, higher loading improves EE% and enables meaningful release kinetics. Above that window, drug crystallization/phase separation can occur, widening PDI and compromising stability and reproducibility.

Maltodextrin (% w/v) (D) serves as the solid carrier for proniosomes, converting the lipid film into a free-flowing, easily hydrated powder, improving handling and scalability. Adequate maltodextrin promotes rapid, complete hydration to niosomes and reduces aggregation; excessive levels can increase particle size (bulking effect) and slow hydration, while too little can impair flow and content uniformity.

Varying A–D in a factorial design allows mapping of main effects and interactions that control EE%, particle size, PDI, and release, enabling selection of a composition that balances tight bilayers (A/B), practical drug loading (C), and robust powder processing/hydration (D) for a stable, reproducible, and scalable proniosomal system.

Sixteen experimental runs were conducted (Table 1), varying each CPP at two levels (-1, +1). Results showed particle sizes ranging from 393.54 to 638.12 nm, with Run 1 yielding the smallest size. PDI ranged from 0.21 to 0.52, with optimal values in Runs 1 and 14. The highest EE% (85.2%) was observed in Run 9 with elevated cholesterol and tenofovir levels, while lower Span 60 or cholesterol levels, as in Runs 4 and 6, led to reduced encapsulation.

3.1. Particle size

The particle size of the various formulations ranged from 393.54 nm to 638.12 nm, with an overall mean size of 504.65 ± 80.35 nm. An analysis of variance (ANOVA) for the particle size response (Y1) indicated that the model was highly significant, with an F-value of 558.64 and a p-value of less than 0.0001 (Table 2.). These values confirm that the variability in particle size was predominantly due to the formulation variables rather than random experimental error.

All four independent variables – Span 60 (A), cholesterol (B), tenofovir (C), and maltodextrin (D) – had a statistically significant impact on particle size. Among

Table 1. Full factorial design with observed responses.

Run	Span60 A (mg)	Cholesterol B (mg)	Tenofovir C (mg)	Maltodextrin D (mg)	Particle size (nm)			PDI			Encapsulation efficiency (%)		
					Actual Value	Predicted Value	Residual	Actual Value	Predicted Value	Residual	Actual Value	Predicted Value	Residual
1	30	10	50	100	393.54	396.18	-2.64	0.21	0.2225	-0.0125	72.08	71.93	0.1538
2	30	20	100	200	600.28	600.82	-0.54	0.46	0.475	-0.015	81.60	81.74	-0.1425
3	30	10	50	200	510.12	507.36	2.76	0.34	0.335	0.005	68.26	68.45	-0.1900
4	15	10	50	200	563.92	566.55	-2.63	0.4	0.41	-0.01	64.53	64.72	-0.1887
5	30	10	100	200	547.12	550.3	-3.18	0.43	0.4275	0.0025	80.32	80.26	0.0575
6	15	20	50	200	581.48	576.99	4.49	0.45	0.4575	-0.0075	63.86	64.31	-0.4513
7	15	20	100	200	638.12	643.02	-4.9	0.52	0.495	0.025	78.12	78.01	0.1088
8	15	20	50	100	411.28	412.11	-0.83	0.34	0.345	-0.005	68.12	67.79	0.3325
9	30	20	100	100	474.26	470.06	4.2	0.36	0.3625	-0.0025	85.20	85.22	-0.0187
10	15	10	100	100	461.27	464.19	-2.92	0.34	0.335	0.005	79.64	80.01	-0.3675
11	30	10	100	100	442.18	439.12	3.06	0.33	0.315	0.015	83.76	83.74	0.0213
12	30	20	50	200	535.74	534.79	0.95	0.41	0.3825	0.0275	68.56	68.04	0.5175
13	15	20	100	100	479.38	478.14	1.24	0.38	0.3825	-0.0025	81.54	81.49	0.0525
14	30	20	50	100	399.43	404.04	-4.61	0.25	0.27	-0.02	71.12	71.52	-0.3987
15	15	10	100	200	612.53	609.49	3.04	0.42	0.4475	-0.0275	76.82	76.53	0.2887
16	15	10	50	100	423.76	421.25	2.51	0.32	0.2975	0.0225	68.42	68.19	0.2250

them, maltodextrin exhibited the most pronounced effect, with a sum of squares (SS) of 76,204.98 and an F-value of 3,522.45. Interaction effects were also notable; the interaction terms AB (Span 60 an- 6 -d cholesterol), AD (Span 60 and maltodextrin), BC (cholesterol and tenofovir), and BD (cholesterol and maltodextrin) were all statistically significant. For example, the interaction between Span 60 and maltodextrin (AD) had an F-value of 53.84, suggesting a strong synergistic influence on particle size.

The model demonstrated excellent fit and predictive ability, as indicated by several key statistical parameters. The coefficient of determination (R^2) was 0.9984, indicating that 99.84% of the variability in particle size was explained by the model. The adjusted R^2 (0.9966) and predicted R^2 (0.9918) were both very close to the actual R^2, confirming model reliability and minimal overfitting. Furthermore, a low coefficient of variation (%CV) of 0.92% and a high Adequate Precision value of 70.758 underscored the precision and robustness of the model.

The polynomial regression equation (Equation 2) shows that Span 60 had a negative effect on particle size, reducing it by approximately 16.82 units, likely due to its surfactant properties that facilitate the formation of smaller vesicles. In contrast, cholesterol, tenofovir, and particularly maltodextrin had positive coefficients, indicating that higher levels of these components led to increased particle sizes. Maltodextrin had the most substantial individual effect, increasing particle size by 69.01 units. Interaction terms such as AD and BD, although smaller in magnitude, also contributed meaningfully to variations in size.

$$\text{Particle size} = 504.65 - 16.82\,A + 10.35\,B + 27.24\,C + 69.01\,D + 4.25\,AB - 8.53\,AD + 5.77\,BC + 4.90\,BD \quad (2)$$

Diagnostic evaluations of the model further validated its reliability. Residual analysis (Table 1) revealed small, normally distributed residuals with no outliers, confirming homoscedasticity and model adequacy. Leverage and Cook's distance values were low, indicating that no single observation unduly influenced the model. Only a few runs, such as Runs 7 and 14, showed slightly elevated residuals, but all values remained within acceptable ranges.

The graphical representations clearly support the statistical analysis of the formulation factors affecting particle size. The perturbation plot in Fig. 1A depicts the individual effects of Span 60 (A), cholesterol (B), tenofovir (C), and maltodextrin (D) on particle size. Span 60 (green line) shows a mild negative effect, suggesting that its surfactant properties reduce surface tension and stabilize smaller particles. Cholesterol (blue line) has a near-neutral effect, indicating its role in membrane rigidity does not significantly impact particle size. Tenofovir (black line) similarly shows minimal influence, reflecting its function primarily as a drug component rather than a structural modifier. In contrast, maltodextrin (purple line) exhibits a strong positive correlation with particle size, likely due to its bulking and stabilizing effects that promote larger particle formation.

The contour (Fig. 1B) and 3D response surface plots (Fig. 1C) illustrate the interactive effects of Span 60 and cholesterol on particle size. Both plots reveal that particle size is minimized (~393.54 nm) at low levels of these components and increases sharply to about 638.12 nm at higher concentrations. The steep gradient in the response surface highlights the strong combined influence of Span 60 and cholesterol, underscoring the need to carefully optimize their levels to maintain desirable particle size and physicochemical properties.

Similarly, the contour (Fig. 1D) and 3D response surface plots (Fig. 1E) demonstrate the interaction between Span 60 and maltodextrin. Particle size remains low when both are at minimal levels but rises significantly to around 638.12 nm as their amounts increase. The gradual increase emphasizes the importance of balancing Span 60 and maltodextrin to control particle size and optimize formulation characteristics.

Figs. 1F and 1G present the combined effects of cholesterol and tenofovir on particle size. Particle size stays minimal (~393.54 nm) at low concentrations but increases steadily to approximately 638.12 nm as both factors rise. This trend highlights their joint impact and the necessity of optimizing their levels to control particle size effectively.

Finally, the contour and 3D plots in Figs. 1H and 1I illustrate the interaction between cholesterol and maltodextrin. Particle size is lowest at minimal levels (~393.54 nm) but increases sharply to about 638.12 nm with higher concentrations of both components. This consistent pattern emphasizes the critical interplay between cholesterol and maltodextrin, reinforcing the importance of balancing these factors for optimal particle size control and formulation stability.

3.2. Polydispersity Index

The polydispersity index (PDI) values in the factorial design ranged from 0.21 to 0.52. ANOVA results (Table 2) show the model is highly significant ($F = 45.44$, $p < 0.0001$), indicating a strong factor influence on PDI. Span 60 (A), cholesterol (B), tenofovir (C), and maltodextrin (D) all significantly affect PDI ($p < 0.001$), with maltodextrin having the greatest impact (sum of squares = 0.0506, $F = 129.81$). The interaction between Span 60 and tenofovir (AC) is also significant ($p = 0.0193$). The low residual error (sum of squares = 0.0039) confirms a good model fit.

Key metrics further support the model's reliability: a low standard deviation (0.0197), mean PDI of 0.3725, and a coefficient of variation of 5.3%, indicating high precision. The close predicted R^2 (0.8921) and adjusted R^2 (0.9368) values show consistent predictive power. An Adeq Precision ratio of 22.533, well above the threshold of 4, confirms a strong signal-to-noise ratio and robust model performance. Overall, the model reliably predicts PDI based on the selected factors and highlights their critical roles in controlling particle size distribution.

The polynomial equation (Equation 3) for PDI shows how key factors influence particle size distribution. The constant term (0.3725) is the average PDI at central factor levels. Span 60 (A) has a negative coefficient (-0.02375), indicating it slightly reduces PDI and promotes uniformity. Cholesterol (B) and tenofovir (C) have positive coefficients (0.02375 and 0.0325), suggesting they slightly

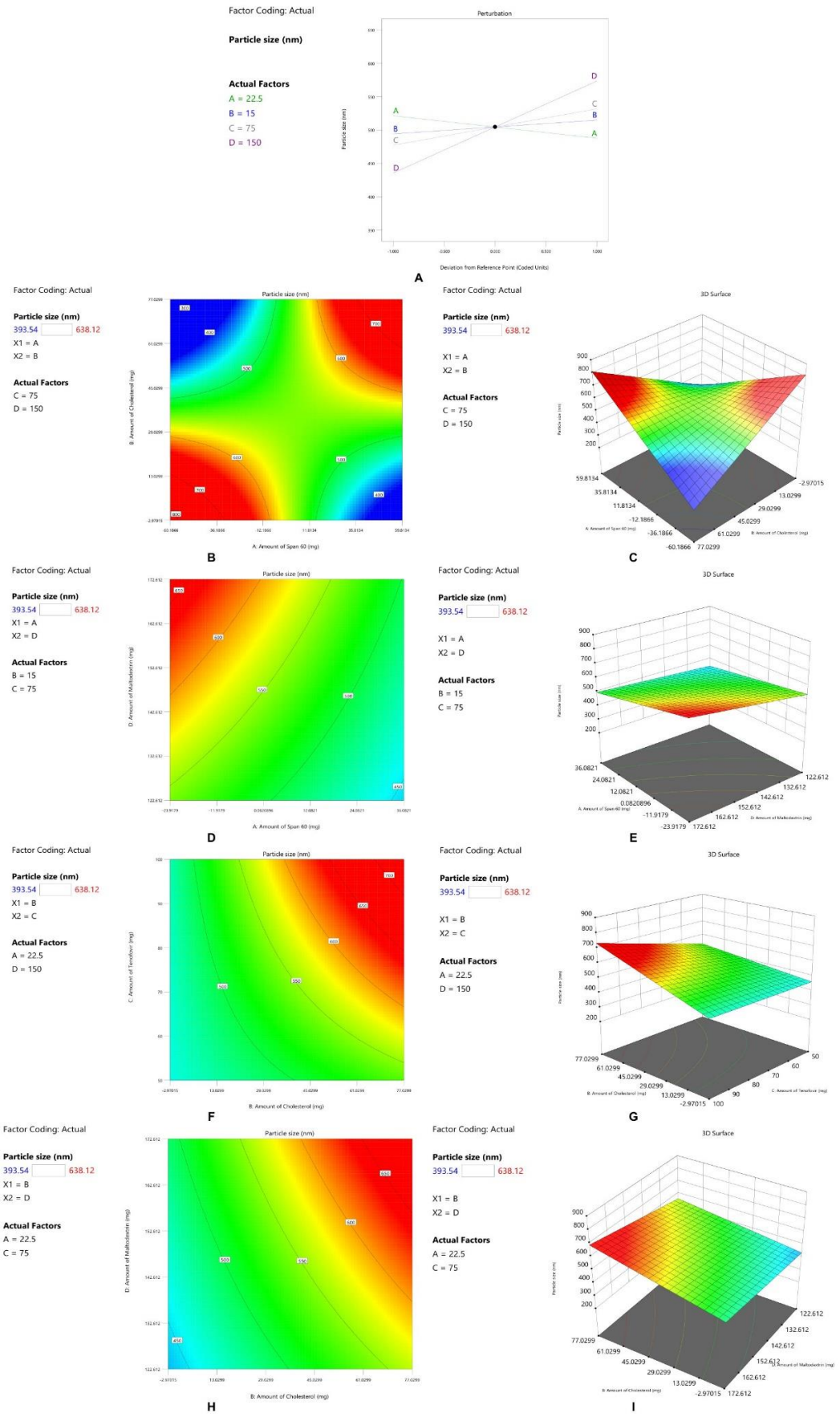

Fig. 1. Effects of formulation variables on particle size: A. Perturbation plot of Span 60 (A), cholesterol (B), tenofovir (C), and maltodextrin (D). B–C. Contour and 3-D plots for Span 60 (A) and cholesterol (B). D–E. Contour and 3-D plots for Span 60 (A) and maltodextrin (D). F–G. Contour and 3-D plots for cholesterol (B) and tenofovir (C). H–I. Contour and 3-D plots for cholesterol (B) and maltodextrin (D).

Table 2. ANOVA Summary for Factorial Models of Particle Size (Y1), Polydispersity Index (Y2), and Encapsulation Efficiency (Y3).

Source	Sum of Squares	df	Mean Square	F-value	p-value	
Particle Size (Y1)						
Model	96686.26	8	12085.78	558.64	< 0.0001	significant
A-Amount of Span 60	4524.92	1	4524.92	209.16	< 0.0001	
B-Amount of cholesterol	1712.51	1	1712.51	79.16	< 0.0001	
C-Amount of tenofovir	11873.92	1	11873.92	548.85	< 0.0001	
D-Amount of maltodextrin	76204.98	1	76204.98	3522.45	< 0.0001	
AB	288.75	1	288.75	13.35	0.0081	
AD	1164.69	1	1164.69	53.84	0.0002	
BC	533.03	1	533.03	24.64	0.0016	
BD	383.47	1	383.47	17.73	0.004	
Residual	151.44	7	21.63			
Cor Total	96837.7	15				
Polydispersity index (Y2)						
Model	0.0886	5	0.0177	45.44	< 0.0001	significant
A-Amount of Span 60	0.009	1	0.009	23.14	0.0007	
B-Amount of cholesterol	0.009	1	0.009	23.14	0.0007	
C-Amount of tenofovir	0.0169	1	0.0169	43.33	< 0.0001	
D-Amount of maltodextrin	0.0506	1	0.0506	129.81	< 0.0001	
AC	0.003	1	0.003	7.76	0.0193	
Residual	0.0039	10	0.0004			
Cor Total	0.0925	15				
Encapsulation Efficiency (Y3)						
Model	759.63	5	151.93	1327.54	< 0.0001	significant
A-Amount of Span 60	55.69	1	55.69	486.62	< 0.0001	
B-Amount of cholesterol	1.15	1	1.15	10.05	0.0100	
C-Amount of tenofovir	650.89	1	650.89	5687.53	< 0.0001	
D-Amount of maltodextrin	48.34	1	48.34	422.38	< 0.0001	
BC	3.56	1	3.56	31.13	0.0002	
Residual	1.14	10	0.1144			
Cor Total	760.77	15				

increase PDI. Maltodextrin (D) has the largest positive effect (0.05625), significantly raising PDI. The interaction between Span 60 and tenofovir (AC) also slightly increases PDI (0.01375).

$$\mathrm{PDI} = 0.3725 - 0.0238\,\mathrm{A} + 0.0238\,\mathrm{B} + 0.0325\,\mathrm{C} + 0.0563\,\mathrm{D} - 0.0138\,\mathrm{AC} \quad (3)$$

The observed and predicted PDI values show a strong model fit, with minimal residuals indicating close agreement. Leverage values are consistent, meaning each data point contributes evenly. Studentized residuals identify Runs 7, 12, and 15 as slightly more influential, but Cook's distance and DFFITS confirm their impact is within acceptable limits. Overall, the model reliably predicts PDI with few significant outliers, validating its accuracy in capturing the effects of key process parameters on particle size distribution.

The perturbation plot in Fig. 2A shows the impact of Span 60 (A), cholesterol (B), tenofovir (C), and maltodextrin (D) on the polydispersity index (PDI). Tenofovir (C) and maltodextrin (D) exhibit steeper slopes, indicating a stronger influence on PDI, with D showing the most pronounced effect. Increasing maltodextrin significantly raises the PDI, while Span 60 (A) and cholesterol (B) have minimal impact. These findings underscore the need to carefully control tenofovir and maltodextrin levels to optimize PDI, ensuring better stability and uniformity of the proniosomal formulation. Figs. 2B and 2C depict the interactive effects of Span 60 (A) and cholesterol (B) on the polydispersity index (PDI). The contour and 3D surface plots show that PDI is minimized (~0.21) at low levels of both components and increases (~0.52) with higher cholesterol and lower Span 60. The steep gradient highlights cholesterol's stronger impact. These results suggest that optimizing the balance between Span 60 and cholesterol is key to achieving a lower, more desirable PDI.

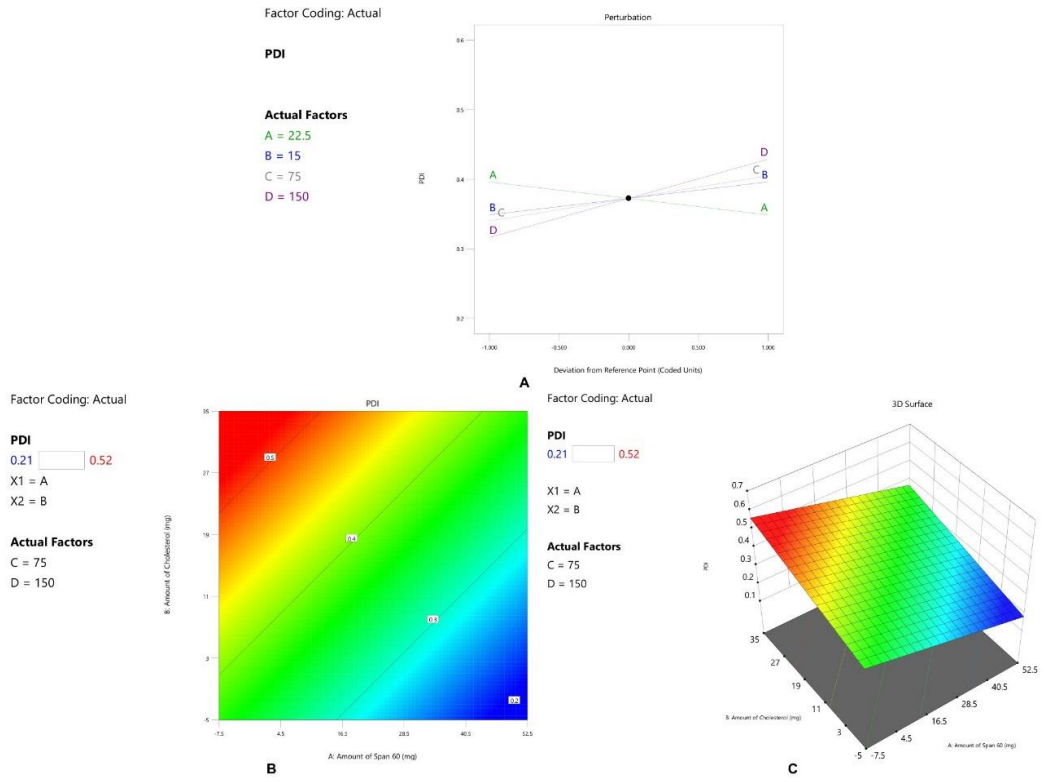

Fig. 2. Effects of formulation variables on PDI: A. Perturbation plot of Span 60 (A), cholesterol (B), tenofovir (C), and maltodextrin (D). B–C. Contour and 3-D plots for Span 60 (A) and tenofovir (C).

3.3. Encapsulation Efficiency

Encapsulation efficiency ranged from 63.86% to 85.2%, with a mean of 74.51% and a standard deviation of 1.33%. ANOVA results show the model is highly significant ($F = 1327.54$, $p < 0.0001$), confirming its robustness. Span 60 (A), cholesterol (B), tenofovir (C), maltodextrin (D), and the interaction between cholesterol and tenofovir (BC) significantly influence encapsulation efficiency (all $p < 0.05$). Tenofovir and Span 60 had the strongest effects ($F = 5687.53$ and 486.62, respectively). These findings highlight the critical role of formulation variables – especially Span 60 and tenofovir – in determining encapsulation efficiency.

The statistical analysis of the encapsulation efficiency (Y3) model confirms strong predictive accuracy and fit. A low standard deviation (0.3383) and high R^2 (0.9985) indicate that 99.85% of the variability is explained by the model. The close alignment of adjusted R^2 (0.9977) and predicted R^2 (0.9961) reinforces its reliability. A low coefficient of variation (0.4541%) reflects high precision, while the Adeq Precision of 100.924 – well above the threshold of 4 – demonstrates an excellent signal-to-noise ratio. Overall, the model is highly robust for optimizing encapsulation efficiency.

The polynomial equation (Equation 4) defines how formulation variables affect encapsulation efficiency. Span 60 (A) and tenofovir (C) have strong positive effects, with coefficients of +1.8656 and +6.3781, respectively, indicating that higher levels significantly boost encapsulation. Cholesterol (B) has a smaller positive effect (+0.2681), suggesting a modest contribution. Maltodextrin (D) shows a negative impact (−1.7381), meaning increased amounts reduce efficiency. The BC interaction term (+0.4719) suggests a mild synergistic effect between cholesterol and tenofovir. Overall, tenofovir and Span 60 are key enhancers, while maltodextrin must be carefully controlled.

$$\text{Encapsulation efficiency (\%)} = 74.50 + 1.87\,A + 0.2681\,B + 6.38\,C - 1.74\,D + 0.4719\,BC \quad (4)$$

Table 2 presents the observed and predicted encapsulation efficiency (Y3) values, along with residuals and diagnostic metrics. The small residuals indicate a strong model fit, while consistent leverage values (0.375) suggest balanced data influence. Most studentized residuals fall within acceptable limits, supporting model reliability. Although Runs 6, 10, and 12 show slightly higher Cook's Distance and DFFITS values, the predicted values align closely with actual results, confirming the model's robustness across varying conditions.

The perturbation plot in Fig. 3A shows how small changes in formulation factors affect encapsulation efficiency. Tenofovir (C) has the greatest impact, as indicated by its steep slope. Span 60 (A) and maltodextrin (D) also influence efficiency, while cholesterol (B) has a minor effect. These results highlight the importance of optimizing tenofovir levels to enhance drug encapsulation. The contour and 3-D response surface plots in Fig. 3B and 3C illustrate the combined effects of cholesterol (B) and tenofovir (C) on encapsulation efficiency. Efficiency is lowest (~63.86%) at low levels of both factors and increases significantly – up to 85.2% – as their levels rise. The steep gradient in the 3-D plot highlights their strong synergistic influence, underscoring the need to optimize both for maximum encapsulation.

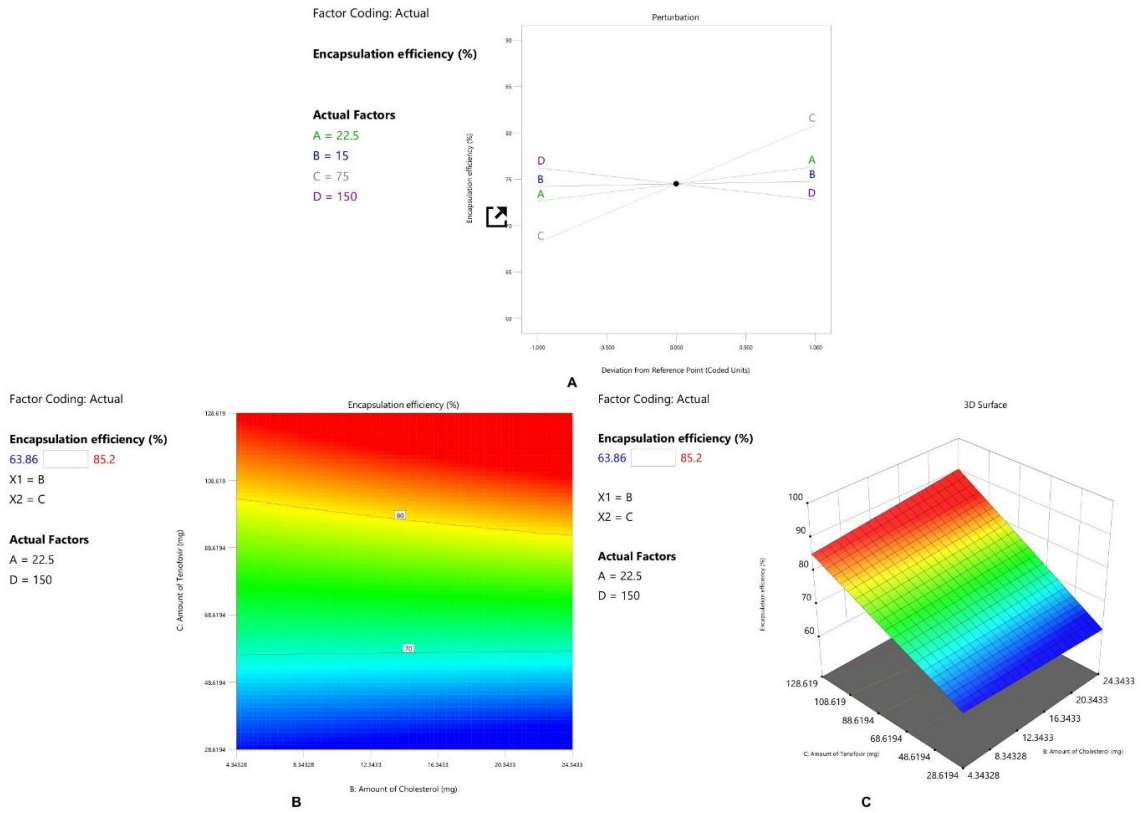

Fig. 3. Effects of formulation variables on encapsulation efficiency: A. Perturbation plot of Span 60 (A), cholesterol (B), tenofovir (C), and maltodextrin (D). B-C. Contour and 3-D plots for cholesterol (B) and tenofovir (C).

3.4. Optimization Using Derringer's Desirability Approach

The formulation was optimized using Derringer's Desirability approach, which applies constraints to each response variable to achieve a balanced and desirable outcome [33].

The selected optimal solution (Solution 1) met all target criteria, yielding a predicted particle size of 418.613 nm, a PDI of 0.2708, and an encapsulation efficiency of 78.0951%, with an overall desirability score of 0.8033.

The optimized formulation consisted of Span 60 (A) at 30.00 mg, cholesterol (B) at 10.00 mg, tenofovir (C) at 76.11 mg, and maltodextrin (D) at 100.00 mg. These levels produced predicted values that fell within acceptable confidence intervals, confirming the effectiveness of the optimization in achieving desirable physicochemical properties.

To validate the model, confirmation experiments were conducted using the optimized conditions. The experimental results closely aligned with the predictions: particle sizes of 423.73 nm, 427.12 nm, and 421.18 nm; PDI values of 0.29, 0.31, and 0.28; and encapsulation efficiencies of 78.12%, 76.12%, and 78.36%, respectively. These results confirm the accuracy and robustness of the model, with all experimental values falling within the predicted confidence intervals, reinforcing the reliability of the design space and process parameters.

3.5. Characterization of Tenofovir-loaded Proniosomal Formulations

Table 3 summarizes the physicochemical properties of three tenofovir-loaded proniosomal formulations (F1, F2, and F3) alongside a blank proniosome. Vesicle sizes ranged from 421.18 ± 11.32 nm in F3 to 427.12 ± 9.67 nm in F2, with the blank proniosomes showing a slightly smaller size of 408.35 ± 8.73 nm. The polydispersity index (PDI), reflecting the uniformity of vesicle size distribution, ranged between 0.28 ± 0.02 for F3 and 0.31 ± 0.01 for F2. The blank proniosomes had a lower PDI of 0.24 ± 0.01, indicating greater homogeneity. Zeta potential (ZP) values, indicating vesicle surface charge and colloidal stability, varied from -22.53 ± 0.78 mV for F2 to -25.52 ± 0.96 mV for F3. The higher magnitude of ZP in F3 suggests enhanced electrostatic repulsion and improved stability. Encapsulation

Table 3. Physicochemical characteristics of tenofovir proniosomes.

Formulation code	Vesicle size (nm)	PDI	ZP (mV)	EE (%)	Vol. of hydration in mL	Time of hydration in minutes	Drug content (%)
F1	423.73 ± 12.54	0.29 ± 0.01	- 24.32 ± 0.62	78.12 ± 4.2	7.3 ± 0.6	8.2 ± 0.6	99.23 ± 2.12
F2	427.12 ± 9.67	0.31 ± 0.01	-22.53 ± 0.78	76.12 ± 3.7	11.9 ± 0.4	7.6 ± 0.8	98.78 ± 1.32
F3	421.18 ± 11.32	0.28 ± 0.02	-25.52 ± 0.96	78.36 ± 3.2	6.9 ± 0.7	7.1 ± 0.5	99.08 ± 1.08
Blank proniosomes	408.35 ± 8.73	0.24 ± 0.01	-21.76 ± 0.58	--	10.6 ± 0.5	6.9 ± 0.6	--

efficiency (EE%) was highest in F3 at 78.36 ± 3.2%, followed by F1 and F2, with F2 exhibiting the lowest efficiency of 76.12 ± 3.7%.

The volume of hydration required for the proniosomes differed among formulations, with F3 needing the least volume (6.9 ± 0.7 mL) and F2 requiring the most (11.9 ± 0.4 mL). Hydration time showed minor variation, ranging from 7.1 ± 0.5 minutes for F3 to 8.2 ± 0.6 minutes for F1. Drug content was consistently high across all drug-loaded formulations, ranging from 98.78 ± 1.32% in F2 to 99.23 ± 2.12% in F1, demonstrating efficient drug loading. While blank proniosomes do not contain the drug, their vesicle size, PDI, and hydration characteristics followed similar trends to the drug-loaded formulations. This comparison highlights the effect of drug incorporation on the physicochemical attributes of the proniosomes.

Fig. 4 illustrates the morphological characteristics of both blank and tenofovir-loaded proniosomes (F1) using optical microscopy (A & B), SEM (C & D), and TEM (E & F). The optical microscopy images (Fig. 4A and 4B) show that both blank and tenofovir-loaded proniosomes are spherical with uniform size distribution. The vesicles are well-dispersed, indicating good formulation stability. Notably, the tenofovir-loaded proniosomes (Fig. 4B) appear more densely packed compared with the blank formulation (Fig. 4A), suggesting effective drug encapsulation within the vesicles. Scanning electron microscopy (SEM) images (Fig. 4C and 4D) further confirm the spherical morphology of both blank and drug-loaded proniosomes. The surface of the blank proniosomes appears smooth and homogeneous, while the tenofovir-loaded vesicles retain a similar shape with a slight increase in size, which can be attributed to drug incorporation. This consistency in morphology supports the structural integrity of the vesicles upon drug loading. Transmission electron microscopy (TEM) images (Fig. 4E and 4F) provide a nanoscale view of the vesicles. Both blank and tenofovir-loaded proniosomes display clearly defined spherical structures with stable boundaries. The Tenofovir-loaded proniosomes are slightly larger and exhibit enhanced contrast, further supporting successful drug encapsulation. These micrographs validate the effective formation of uniformly distributed and stable proniosomes suitable for drug delivery applications.

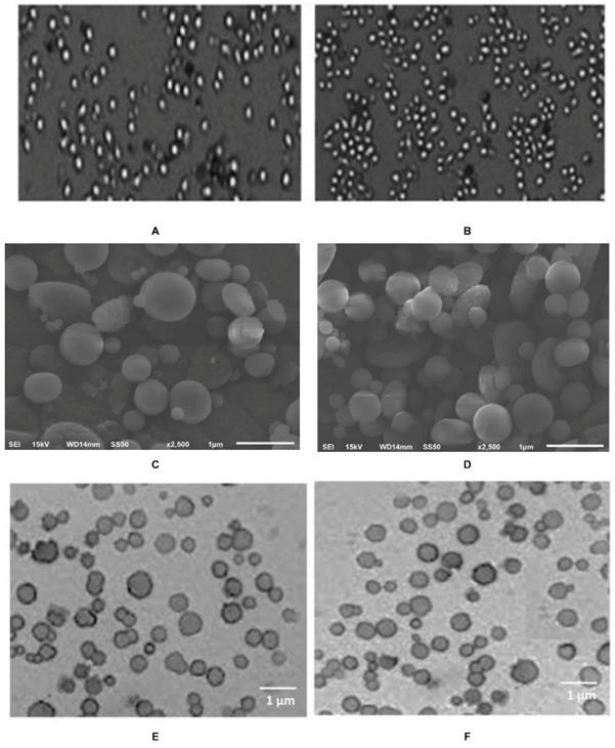

Fig. 4. Morphological characterization of proniosomes. Optical microscopy images: (A) Blank proniosomes and (B) Tenofovir-loaded proniosomes. Scanning electron microscopy (SEM) images: (C) Blank proniosomes and (D) Tenofovir-loaded proniosomes. Transmission electron microscopy (TEM) images: (E) Blank proniosomes and (F) Tenofovir-loaded proniosomes.

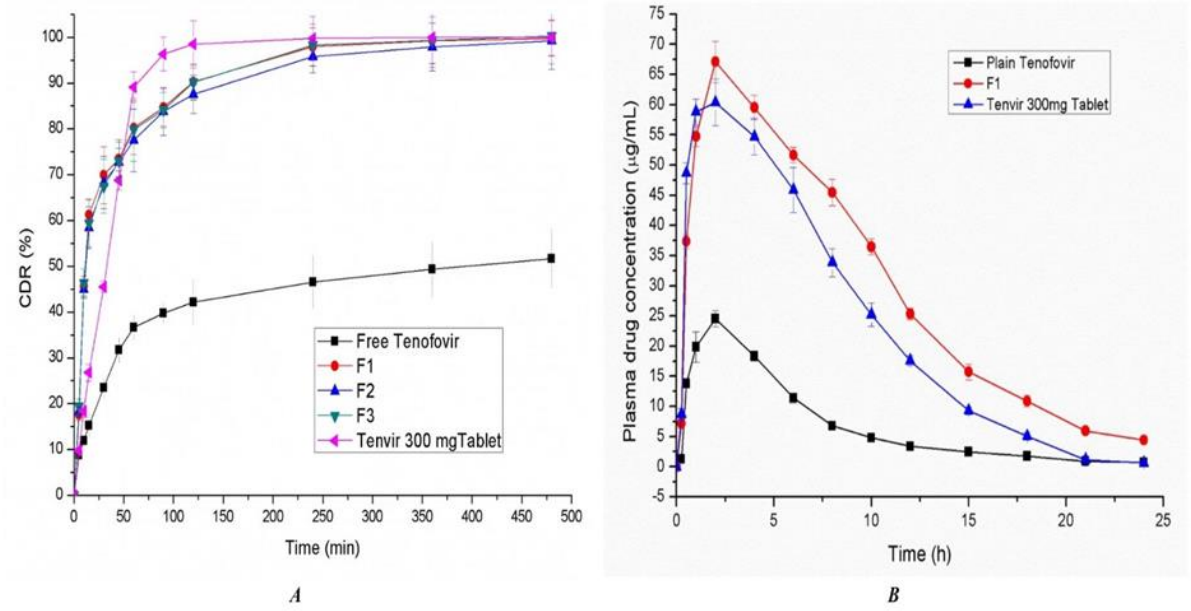

Fig. 5. (A) Cumulative drug release (CDR) profiles of three proniosomal formulations (F1, F2, and F3) compared with free tenofovir and a marketed Tenvir® 300 mg tablet in simulated intestinal fluid. All three proniosomal formulations exhibited similar release patterns. (B) Plasma concentration–time profile of tenofovir following oral administration in rats for the optimized formulation (F1) versus free tenofovir.

Table 4. Drug release kinetics of tenofovir optimized formulation.

Formulation Code	Zero Order		First Order		Higuchi		Korsmeyer-Peppas	
	R^2	n	R^2	n	R^2	n	R^2	N
F1	0.4039	0.1399	0.9691	-0.0052	0.6737	3.9593	0.9013	37.6887

The dissolution profile of tenofovir from maltodextrin-based proniosomes, illustrated in Fig. 5, highlights the cumulative drug release (CDR) over 480 minutes and compares five formulations: free tenofovir, F1, F2, F3, and the marketed Tenvir 300 mg tablet. Free tenofovir exhibited the slowest release, achieving only 51.69% CDR by the end of the study, suggesting limited dissolution and potentially reduced bioavailability. In contrast, the proniosomal formulations (F1, F2, and F3) showed markedly faster and more efficient drug release, all surpassing 90% CDR within the first 120 minutes. Among them, F1 achieved 99.78% release, while F2 and F3 reached 99.23% and 100.32%, respectively, demonstrating their capability for enhanced drug delivery. The marketed Tenvir tablet also showed a robust release profile, achieving 99.96% CDR at 480 minutes – comparable to the proniosomal formulations. These findings indicate that maltodextrin-based proniosomes significantly improve Tenofovir release, offering an effective alternative to conventional formulations.

Table 4 presents the drug release kinetics of tenofovir from the optimized formulation (F1), analyzed using various mathematical models: zero-order, first-order, Higuchi, and Korsmeyer-Peppas. The zero-order model showed a poor fit with an R^2 of 0.4039 and a slope of 0.1399, indicating a slow, non-ideal release pattern. In contrast, the first-order model exhibited an excellent fit (R^2 = 0.9691; slope = -0.0052), suggesting that the release rate is concentration-dependent. The Higuchi model, which characterizes drug release through diffusion, had a moderate fit (R^2 = 0.6737; slope = 3.9593). The Korsmeyer-Peppas model also showed a strong fit (R^2 = 0.9013; slope = 37.6887), indicating that the release mechanism likely involves both diffusion and matrix erosion. Overall, the results suggest that tenofovir release from the optimized proniosomal formulation follows primarily first-order kinetics with a significant contribution from diffusion-controlled mechanisms.

The angle of repose data provides insight into the flowability of various formulations. Maltodextrin exhibited a relatively high angle of repose (47.38° ± 0.71°), indicating poor flow characteristics, while the physical mixture showed an even higher value (53.27° ± 0.83°), reflecting suboptimal flow. In contrast, the F3 formulation demonstrated a significantly lower angle of repose (32.76° ± 0.56°), suggesting improved flow behavior. The blank proniosomes exhibited the best flowability, with the lowest angle of repose recorded at 31.19° ± 0.51°. These findings indicate that proniosomal formulations possess superior flow properties compared to raw materials and physical mixtures, likely due to their spherical morphology and uniform particle size, which reduce interparticle friction.

Fig. 6. shows the DSC thermograms of free tenofovir, the physical mixture, tenofovir-loaded proniosomes, and blank proniosomes. Free tenofovir exhibits a sharp endothermic peak at 279.6°C, confirming its crystalline nature. The physical mixture shows a similar peak at 278.2°C, along with a minor peak at 123.5°C, likely due to excipient transitions. In contrast, the tenofovir-loaded proniosomes display a markedly reduced tenofovir peak, suggesting drug encapsulation or conversion to an amorphous state. Blank proniosomes show no significant thermal events, confirming their amorphous nature. These results indicate that proniosomal encapsulation alters the thermal properties of tenofovir, potentially enhancing its stability and solubility.

The FTIR spectra (Fig. 7) of (A) pure tenofovir, (B) the physical mixture of tenofovir with maltodextrin, and (C) tenofovir-loaded proniosomes were analyzed to evaluate drug-carrier compatibility and encapsulation efficiency. Pure tenofovir exhibited characteristic absorption bands at 3300–3500 cm^{-1} (O–H and N–H stretching), 1600–1650 cm^{-1} (C=C aromatic stretching and

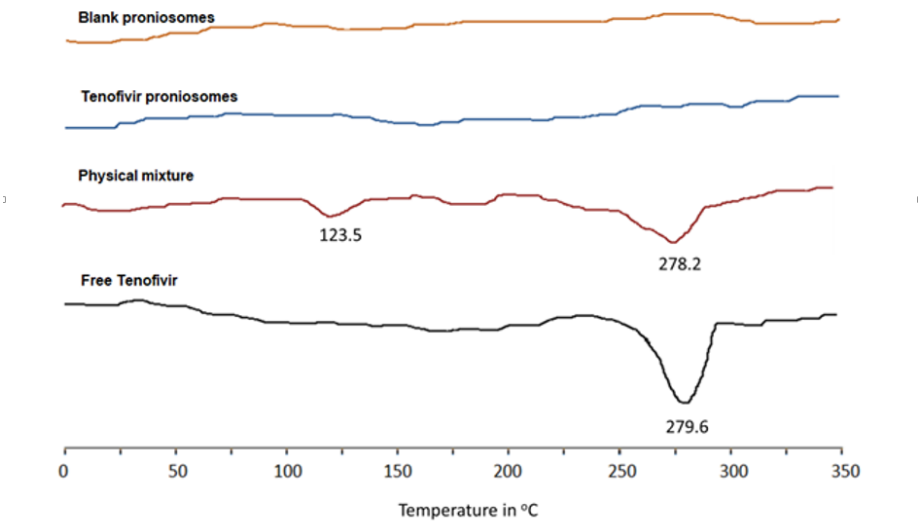

Fig. 6. DSC of (A) Tenofovir, (B) Physical mixture, (C) Tenofovir-loaded proniosomes (D) Blank proniosomes.

N–H bending), 1400–1500 cm^{-1} (C=N stretching from the adenine purine ring), 1200–1300 cm^{-1} (P=O stretching from the phosphonate group), and 1000–1100 cm^{-1} (P–O and C–O stretching vibrations). The physical mixture showed overlapping peaks from both components with enhanced aliphatic C–H stretching (2900–2950 cm^{-1}) due to maltodextrin contribution, while drug characteristic peaks remained intact, indicating minimal molecular interactions and maintained drug stability. In contrast, the proniosome formulation demo nstrated significant spectral modifications including broadening of the O–H stretching region (3200–3500 cm^{-1}), intense aliphatic C–H stretching (2800–2950 cm^{-1}) from lipid components, reduced intensity of tenofovir characteristic peaks, particularly in aromatic (1600–1650 cm^{-1}) and phosphonate regions (1200–1300 cm^{-1}), and complex overlapping in the C–O/P–O stretching region (1000–1200 cm^{-1}). These spectral changes in the proniosome formulation confirm successful drug encapsulation within the niosomal matrix through hydrogen bonding and van der Waals interactions between tenofovir and carrier components, indicating drug-carrier compatibility without chemical degradation and supporting the formulation's potential for enhanced drug delivery applications. Free tenofovir exhibited low uptake (31.3 ± 1.6%), while the F1 proniosomal formulation significantly enhanced uptake to 83.5 ± 4.7%, likely due to improved membrane permeability or sustained release. The physical mixture showed slightly better uptake (34.8 ± 1.9%) than free tenofovir, but still much lower than F1. The commercial Tenvir 300 mg tablet demonstrated higher uptake (73.4 ± 5.7%) than the free drug but was less effective than F1. These findings highlight the superior cellular uptake of the F1 formulation, supporting its potential to improve tenofovir bioavailability.

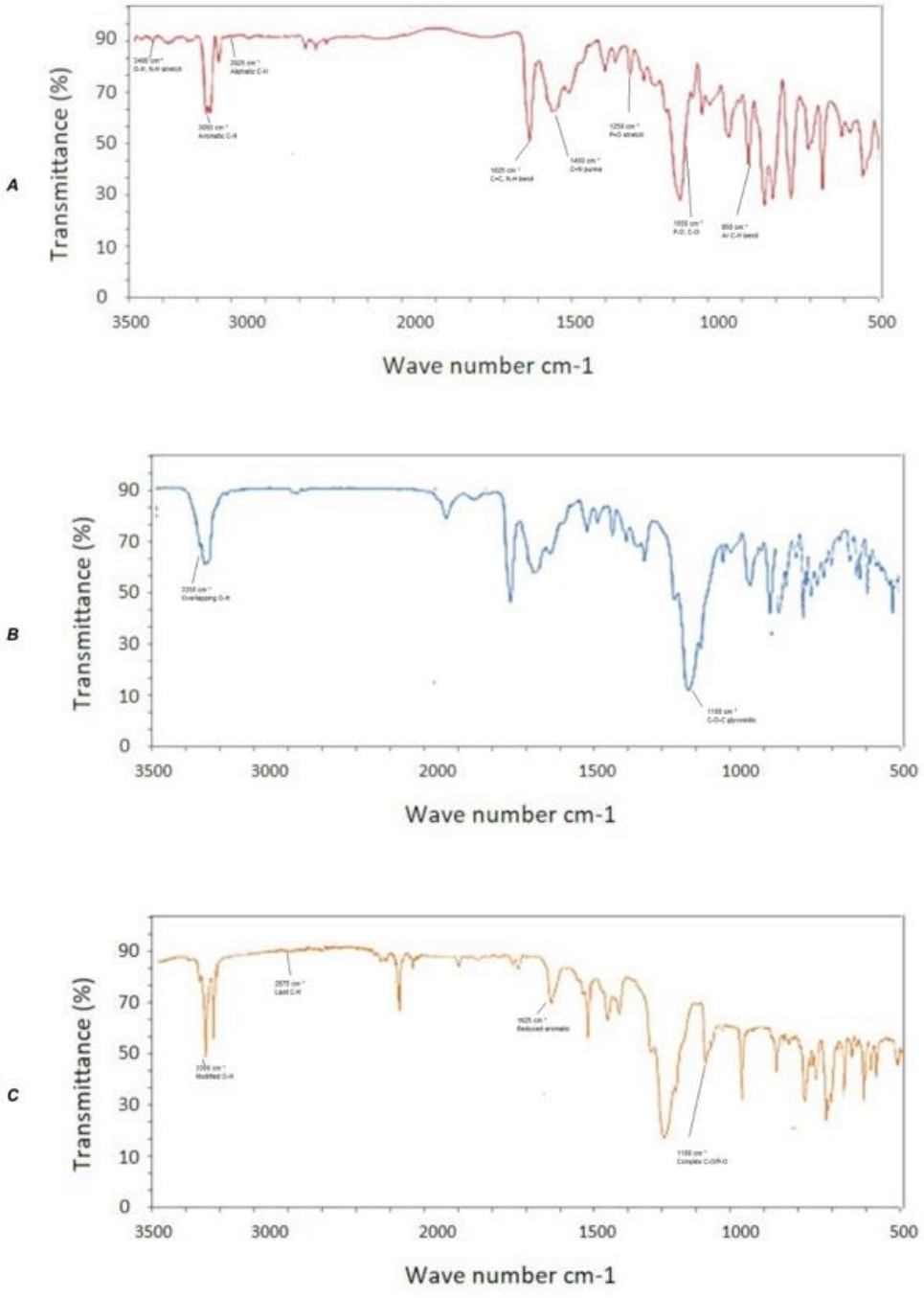

Fig. 7. FTIR of (A) Tenofovir, (B) Physical mixture of tenofovir and maltodextrin, and (C) Tenofovir-loaded proniosomes

Fig. 8A shows the in vitro cellular uptake of tenofovir in NCI-N87 gastric cells from various formulations.

Fig. 8B presents the MDR1 efflux study results using MDCK-MDR1 cells, comparing tenofovir formulations with and without an efflux inhibitor. Free tenofovir showed low transport from apical to basolateral (A to B) direction (15.4 ± 1.1%) without the inhibitor, which increased to 48.4 ± 2.8% in the presence of the inhibitor, indicating strong MDR1-mediated efflux. B to A transport decreased from 12.8 ± 0.9% to 6.3 ± 1.1% with the inhibitor, confirming this effect. The F1 formulation markedly improved A to B transport to 78.54 ± 3.8% without the inhibitor and 84.12 ± 3.7% with it, while B to A transport dropped from 24.12 ± 1.2% to 2.5 ± 0.5%, showing effective MDR1 efflux reduction and enhanced permeability. The physical mixture and Tenvir tablet showed moderate improvements over free tenofovir but were less effective than F1. Overall, F1 demonstrated the greatest potential to overcome MDR1 efflux and boost tenofovir bioavailability.

Fig. 8C shows MDR1 efflux studies in Caco-2 cells, assessing tenofovir transport from apical to basolateral (A to B) and vice versa (B to A), with and without an MDR1 inhibitor. Free tenofovir had low A to B transport (17.8 ± 0.4%) and moderate B to A transport (11.5 ± 0.5%) without the inhibitor. Adding the inhibitor increased A to B transport to 45.64 ± 3.1% and reduced B to A to 6.2 ± 0.7%, indicating active efflux limiting absorption. The F1 proniosomal formulation showed the highest A to B transport without the inhibitor (81.32 ± 4.1%) and a higher B to A transport (24.53 ± 1.4%), suggesting better interaction with cellular transporters. With the inhibitor, A to B transport increased slightly to 86.12 ± 2.9%, while B to A dropped to 2.8 ± 0.9%, confirming efficient efflux bypass. The physical mixture showed moderate transport improvements with the inhibitor but remained less effective than F1. The Tenvir tablet performed better than the physical mixture but was still inferior to F1. Overall, F1 demonstrated superior permeability and the best ability to overcome MDR1 efflux, indicating its potential to enhance Tenofovir's oral bioavailability and therapeutic efficacy.

Fig. 8D shows MTT assay results assessing cytotoxicity of the F1 tenofovir-loaded proniosomes and Tenvir 300 mg tablet across concentrations from 0.1 to 200 µg/mL. Both formulations maintained high cell viability at all concentrations, with F1 showing slightly higher viability (98.58 ± 4.27% at 0.1 µg/mL and 96.18 ± 3.85% at 200 µg/mL) compared to Tenvir (97.68 ± 4.98% and 94.68 ± 5.21%, respectively). These results indicate minimal cytotoxicity and good cell tolerance for both, with F1 demonstrating a marginally better safety profile, supporting their suitability for further development.

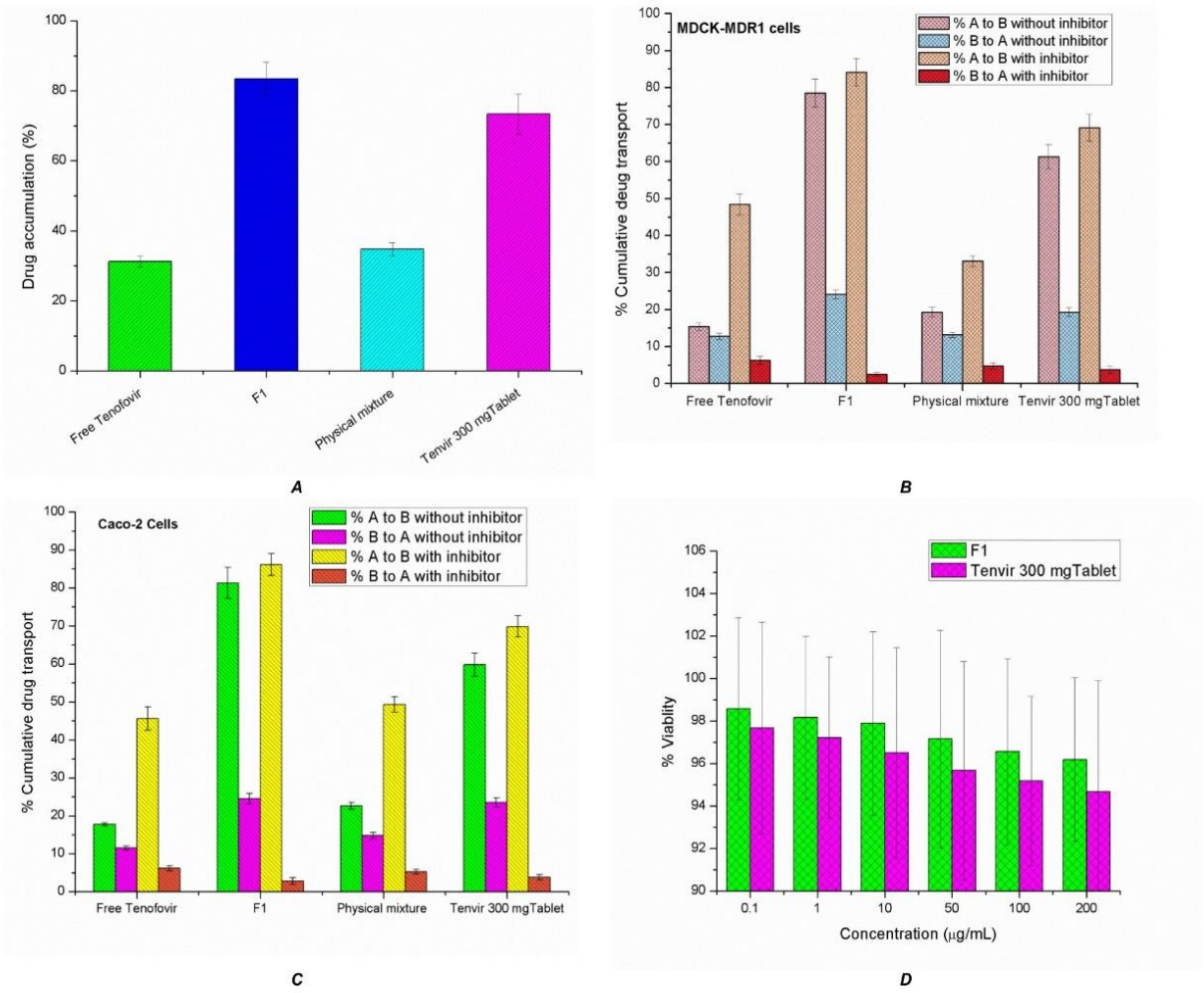

Fig. 8. (A) Results of in vitro cellular uptake study via NCI-N87 gastric cells. (B) Results of MDR1 efflux studies against MDCK-MDR1 cells. (C) Results of MDR1 efflux studies against Caco-2 cells. (D) Results of cytotoxicity determination using MTT assay.

Table 5. Results of accelerated stability study.

Days	4°C (Refrigerated condition)		25°C (Room temperature)		40°C (Accelerated condition)		25°C + Light (ICH Option 2: 1.2M lux·hr)		40°C/75% RH (High humidity condition)	
	Particle size (nm)	Drug content (%)	Particle size (nm)	Drug content (%)	Particle size (nm)	Drug content (%)	Particle size (nm)	Drug content (%)	Particle size (nm)	Drug content (%)
0	423.73 ± 12.54	99.23 ± 2.12	423.73 ± 12.54	99.23 ± 2.12	423.73 ± 12.54	99.23 ± 2.12	423.73 ± 12.54	99.23 ± 2.12	423.73 ± 12.54	99.23 ± 2.12
30	427.12 ± 18.82	98.94 ± 3.37	426.83 ± 17.32	98.72 ± 3.15	429.12 ± 15.32	98.82 ± 3.76	428.45 ± 16.78	98.65 ± 2.89	431.89 ± 19.45	98.43 ± 3.25
60	428.37 ± 15.65	98.65 ± 4.23	428.12 ± 19.12	98.32 ± 4.08	432.12 ± 18.27	98.18 ± 1.97	433.67 ± 20.15	98.08 ± 3.47	436.54 ± 22.89	97.85 ± 4.12
90	429.12 ± 10.78	98.52 ± 3.08	431.54 ± 11.19	98.08 ± 3.35	433.89 ± 12.78	97.38 ± 4.13	437.23 ± 18.92	97.25 ± 2.76	441.87 ± 25.34	96.89 ± 3.89

The comprehensive accelerated stability study results for the tenofovir proniosomal formulation, as presented in Table 5, demonstrate acceptable stability profiles across multiple ICH-recommended storage and stress conditions over 90 days. The study evaluated five distinct conditions: 4°C (refrigerated), 25°C (room temperature), 40°C (accelerated condition), 25°C with light exposure (1.2 million lux hours), and 40°C/75% RH (high humidity). Initially, the particle size was 423.73 ± 12.54 nm across all conditions, which showed minimal increases to 429.12 ± 10.78 nm, 431.54 ± 11.19 nm, and 433.89 ± 12.78 nm after 90 days under refrigerated, room temperature, and accelerated conditions, respectively. More pronounced changes were observed under stress conditions, with particle sizes reaching 437.23 ± 18.92 nm under light exposure and 441.87 ± 25.34 nm under high humidity conditions. Drug content showed corresponding trends, decreasing from the initial 99.23 ± 2.12% to 98.52 ± 3.08%, 98.08 ± 3.35%, and 97.38 ± 4.13% under refrigerated, room temperature, and accelerated conditions, respectively, while photostability testing resulted in 97.25 ± 2.76% drug retention and high humidity conditions showed 96.89 ± 3.89% retention after 90 days. These results indicate that while the formulation demonstrates excellent stability under normal storage conditions with minimal particle size increases (< 2.5%) and drug content retention (> 97%), environmental stress factors such as light and humidity have more significant impacts, though still within acceptable pharmaceutical limits. The comprehensive stability profile confirms the formulation's suitability for pharmaceutical applications with appropriate storage recommendations.

The pharmacokinetic study (Fig. 5B and Table 6) compared three tenofovir formulations: plain tenofovir, tenofovir proniosomes (F1), and Tenvir 300 mg tablets. Key parameters such as C_{max}, AUC, T_{max}, elimination rate constant (K_{el}), and half-life ($t_{1/2}$) were analyzed to evaluate bioavailability and sustained drug release. Plain tenofovir showed the lowest peak plasma concentration (C_{max}) of 24.51 µg/mL at around 2 hours. In contrast, the F1 formulation reached a significantly higher Cmax of 67.12 µg/mL, highlighting enhanced bioavailability. The Tenvir tablets had a C_{max} of 60.37 µg/mL, which was better than the plain drug but slightly lower than F1. These results indicate that both F1 and Tenvir improve drug absorption considerably. The area under the curve (AUC), representing total drug exposure, was much greater for F1 (1457.16 µg·h/mL) and Tenvir (1624.53 µg·h/mL) compared to plain tenofovir (211.45 µg·h/mL). This substantial increase suggests that the F1 and Tenvir formulations provide sustained drug release, prolonging drug availability in the bloodstream. T_{max} values were similar across all formulations, approximately 2 hours, showing no significant difference in the time to reach peak concentration. However, differences were observed in the elimination rate constant (K_{el}) and half-life ($t_{1/2}$). F1 had the lowest K_{el} (0.021 h^{-1}), indicating slower drug elimination compared to plain tenofovir (0.039 h^{-1}) and Tenvir (0.023 h^{-1}). Correspondingly, F1 had the longest half-life (33.15 hours), followed by Tenvir (30.13 hours), with plain tenofovir having the shortest (17.76 hours). This reflects a more controlled and extended release profile for the F1 formulation. The pharmacokinetic parameters demonstrate that both the F1 proniosomal formulation and Tenvir 300 mg tablets significantly enhance the bioavailability and sustained release of tenofovir over the plain drug. Among these, F1 showed a superior ability to maintain higher drug levels for longer and reduce elimination, making it a promising option for improved therapeutic efficacy.

Table 6. Pharmacokinetic parameters of tenofovir in rats (n=6) after administration of 25 mg as a single oral dose of proniosomal formulation and Tenvir.

PK parameter	Plain Tenofovir	Tenofovir proniosomes (F1)	Tenvir 300 mg tablet
C_{max} (µg/ml)	24.51 ± 1.34	67.12 ± 3.41*	60.37 ± 3.84*
AUC(0-78) (µg.h/mL)	194.63 ± 17.23	1362.47 ± 35.41*	1533.76 ± 52.82*
AUC(0-∞) (µg. h/mL)	211.45 ± 14.54	1457.16 ± 37.85*	1624.53 ± 55.46*
T_{max} (h)	2.08 ± 0.07	2.12 ± 0.05	2.06 ± 0.03
K_{el} (h^{-1})	0.039 ± 0.004	0.021 ± 0.003	0.023 ± 0.003
$t_{1/2}$ (h)	17.76 ± 0.73	3315 ± 0.52	30.13 ± 0.48

4. Summary and Conclusion

This study successfully developed and optimized tenofovir-loaded proniosomes using a 2^4 factorial design to systematically evaluate the effects of critical formulation variables, including Span 60, cholesterol, drug load, and maltodextrin, on key quality attributes. The optimized formulation exhibited a vesicle size of ~423 nm, low PDI (<0.3), a zeta potential of -24 mV, and high encapsulation efficiency (~78%), indicating a stable and uniform vesicular system. Microscopy studies confirmed spherical, well-dispersed vesicles with structural integrity. In vitro dissolution studies demonstrated rapid and sustained drug release from proniosomes compared to free tenofovir, with release kinetics best described by the first-order and Korsmeyer–Peppas models, suggesting diffusion-controlled release. Cellular uptake and efflux studies confirmed significantly enhanced permeability and reduced MDR1-mediated efflux for the optimized formulation, while cytotoxicity assays confirmed its safety. Pharmacokinetic evaluation in rats further revealed superior oral bioavailability, higher plasma concentrations, and extended half-life compared to plain tenofovir, aligning closely with the marketed Tenvir® tablet. Stability testing under ICH-recommended conditions confirmed robustness, with minimal changes in particle size and drug content over 90 days. Overall, the findings establish proniosomes as a promising nanocarrier system for improving the delivery of tenofovir. By enhancing solubility, stability, permeability, and bioavailability, the optimized proniosomal formulation holds significant potential to overcome the limitations of conventional tenofovir therapy and to contribute to improved patient outcomes in HIV/AIDS and HBV management.

Author Contributions: Conceptualization, S.A. and A.A.; methodology, S.A.; validation, S.A. and A.A.; investigation, S.A.; resources, A.A.; data curation, A.A.; writing—original draft preparation, S.A.; writing—review and editing, A.A.; visualization, S.A.; supervision, A.A.; project administration, A.A. All authors have read and agreed to the published version of the manuscript.

Funding: We have not received any external funding.

Acknowledgments: The authors express their gratitude to the Department of Pharmaceutics at KL College of Pharmacy, Koneru Lakshmaiah Education Foundation, Vaddeswaram, Andhra Pradesh, India, for the facilities provided to conduct this research work.

Conflicts of Interest: The authors declare that they have no competing interests.

References

1. Menéndez-Arias, L.; Delgado, R. Update and latest advances in antiretroviral therapy. *Trends Pharmacol. Sci.* **2022**, *43(1)*, 16–29. DOI: 10.1016/j.tips.2021.10.004
2. Peng, Y.; Zong, Y.; Wang, D.; Chen, J.; Chen, Z.S.; Peng, F.; Liu, Z. Current drugs for HIV-1: from challenges to potential in HIV/AIDS. *Front. Pharmacol.* **2023**, *14*, Art. No: 1294966. DOI: 10.3389/fphar.2023.1294966
3. Watkins, M.E.; Wring, S.; Randolph, R.; et al. Development of a novel formulation that improves preclinical bioavailability of tenofovir disoproxil fumarate. *J. Pharm. Sci.* **2017**, *106*, 906–919. DOI: 10.1016/j.xphs.2016.12.015
4. Sangeetha, S. Formulation Design, Optimization, and Evaluation of Solid Lipid Nanoparticles Loaded With an Antiviral Drug Tenofovir Using Box–Behnken Design for Boosting Oral Bioavailability. *Adv. Pharmacol. Pharm. Sci.* **2024**, *2024*, Art. No: 5248746. DOI: 10.1155/2024/5248746
5. Limenh, L.W. Advances in the transdermal delivery of antiretroviral drugs. *SAGE Open Med.* **2024**, *12*, Art. No: 20503121231223600. DOI: 10.1177/20503121231223600
6. Burns, R.N.; Hendrix, C.W.; Chaturvedula, A. Population pharmacokinetics of tenofovir and tenofovir-diphosphate in healthy women. J. *Clin. Pharmacol.* **2015**, *55*, 629–638. DOI: 10.1002/jcph.464
7. Hagos, Y.; Wolff, N.A. Assessment of the role of renal organic anion transporters in drug-induced nephrotoxicity. *Toxins* **2010**, *2*, 2055–2082. DOI: 10.3390/toxins2082055
8. Kohler, J.J.; Hosseini, S.H.; Green, E.; et al. Tenofovir renal proximal tubular toxicity is regulated by OAT1 and MRP4 transporters. *Lab. Invest.* **2011**, *91*, 852–858. DOI: 10.1038/labinvest.2011.35
9. Agrahari, V.; Putty, S.; Mathes, C.; et al. Evaluation of degradation kinetics and physicochemical stability of tenofovir. *Drug Test. Anal.* **2015**, *7*, 207–213. DOI: 10.1002/dta.1659
10. De Clercq, E. Tenofovir alafenamide (TAF) as the successor of tenofovir disoproxil fumarate (TDF). *Biochem. Pharmacol.* **2016**, *119*, 1–7. DOI: 10.1016/j.bcp.2016.04.002
11. Murphy, R.A.; Valentovic, M.A. Factors contributing to the antiviral effectiveness of tenofovir. *J. Pharmacol. Exp. Ther.* **2017**, *363*, 156–163. DOI: 10.1124/jpet.117.242073
12. Singireddy, A.R.; Pedireddi, S.R. Advances in lopinavir formulations: strategies to overcome solubility, bioavailability, and stability challenges. *Prospect. Pharm. Sci.* **2024**, *22*, 105–121. DOI: 10.56782/pps.280
13. Cobb, D.A.; Smith, N.; Deodhar, S.; et al. Transformation of tenofovir into stable ProTide nanocrystals with long-acting pharmacokinetic profiles. *Nat. Commun.* **2021**, *12*, Art. No: 5458. DOI: 10.1038/s41467-021-25770-4
14. Safari, J.B.; Bapolisi, A.M.; Krause, R.W. Development of pH-sensitive chitosan-g-poly(acrylamide-co-acrylic acid) hydrogel for controlled drug delivery of tenofovir disoproxil fumarate. *Polymers* **2021**, *13*, Art. No: 3571. DOI: 10.3390/polym13203571
15. Zhang, T.; Zhang, C.; Agrahari, V.; et al. Spray drying tenofovir loaded mucoadhesive and pH-sensitive microspheres intended for HIV prevention. *Antivir. Res.* **2013**, *97*, 334–346. DOI: 10.1016/j.antiviral.2012.12.008

16. Pribut, N.; D'Erasmo, M.; Dasari, M.; et al. ω-Functionalized lipid prodrugs of HIV NtRTI tenofovir with enhanced pharmacokinetic properties. *J. Med. Chem.* **2021**, *64*, 12917–12937. DOI: 10.1021/acs.jmedchem.1c00928

17. Reddy, D.M.; Chetty, C.M.; Reddy, Y.D.; et al. Formulation and Evaluation of fast dissolving buccal patches of tenofovir disoproxil fumarate. *Res. J. Pharm. Technol.* **2021**, *14*, 225–230. DOI: 10.52711/0974-360X.2021.00038

18. Cazorla-Luna, R.; Notario-Pérez, F.; Martín-Illana, A.; et al. Chitosan-based mucoadhesive vaginal tablets for controlled release of the anti-HIV drug tenofovir. *Pharmaceutics* **2019**, *11*, Art. No: 20. DOI: 10.3390/pharmaceutics11010020

19. Belletti, D.; Tosi, G.; Forni, F.; et al. Chemico-physical investigation of tenofovir loaded polymeric nanoparticles. *Int. J. Pharm.* **2012**, *436*, 753–763. DOI: 10.1016/j.ijpharm.2012.06.059

20. Mathieu, T.; Favetta, P.; Agrofoglio, L.A. Molecularly Imprinted Polymeric Nanoparticles as Drug Delivery System for Tenofovir, an Acyclic Nucleoside Phosphonate Antiviral. *Pharmaceutics* **2024**, *16*, Art. No: 965. DOI: 10.3390/pharmaceutics16070965

21. Zidan, A.S.; Spinks, C.B.; Habib, M.J.; et al. Formulation and transport properties of tenofovir loaded liposomes through Caco-2 cell model. *J. Liposome Res.* **2013**, *23*, 318–326. DOI: 10.3109/08982104.2013.814823

22. Spinks, C.B.; Zidan, A.S.; Khan, M.A.; et al. Pharmaceutical characterization of novel tenofovir liposomal formulations for enhanced oral drug delivery: in vitro pharmaceutics and Caco-2 permeability investigations. *Clin. Pharmacol. Adv. Appl.* **2017**, *9*, 29–38. DOI: 10.2147/CPAA.S122449

23. Khatoon, M.; Shah, K.U.; Din, F.U.; et al. Proniosomes derived niosomes: recent advancements in drug delivery and targeting. *Drug Deliv.* **2017**, *24*, 56–69. DOI: 10.1080/10717544.2016.1230054

24. Khindri, S.; Aggarwal, G.; Hari Kumar, S.L. Role of niosomes and proniosomes for enhancing bioavailability of drugs. J. *Drug Deliv. Ther.* **2015**, *5*, 28–33. DOI: 10.22270/jddt.v5i1.1004

25. Song, S.; Tian, B.; Chen, F.; et al. Potentials of proniosomes for improving the oral bioavailability of poorly water-soluble drugs. *Drug Dev. Ind. Pharm.* **2015**, *41*, 51–62. DOI: 10.3109/03639045.2013.865234

26. Ahmed, S.; Farag, M.M.; Attia, H.; et al. Exploring the potential of antifungal-loaded proniosomes to consolidate corneal permeation in fungal keratitis: A comprehensive investigation from laboratory characterization to microbiological evaluation. *Int. J. Pharm. X* **2025**, *9*, Art. No: 100322. DOI: 10.1016/j.ijpx.2024.100322

27. Thongpon, P.; Intuyod, K.; Pongking, T.; et al. Curcumin-Loaded Maltodextrin-Based Proniosomes Potentially Effective against Gemcitabine-Resistant Cholangiocarcinoma. *ACS Appl. Bio Mater.* **2025**, *8*, 913-930. DOI: 10.1021/acsabm.4c01832

28. Anwer, K.E.; El-Sattar, N.E.; Shamaa, M.M.; et al. Design, green synthesis and tailoring of vitamin E TPGS augmented niosomal nano-carrier of pyrazolopyrimidines as potential anti-liver and breast cancer agents with accentuated oral bioavailability. *Pharmaceuticals* **2022**, *15*, Art. No: 330. DOI: 10.3390/ph15030330

29. Paarakh, M.P.; Jose, P.A.; Setty, C.M.; Peterchristoper, G.V. Release kinetics–concepts and applications. *Int. J. Pharm. Res. Technol.* **2018**, *8*, 12–20.

30. Askarizadeh, M.; Esfandiari, N.; Honarvar, B.; et al. Kinetic modeling to explain the release of medicine from drug delivery systems. *ChemBioEng Rev.* **2023**, *10*, 1006–1049. DOI: 10.1002/cben.202300065

31. Atnip, A.; Giusti, M.M.; Sigurdson, G.T.; et al. The NCI-N87 cell line as a gastric epithelial model to study cellular uptake, trans-epithelial transport, and gastric anti-inflammatory properties of anthocyanins. *Nutr. Cancer* **2020**, *72*, 686–695. DOI: 10.1080/01635581. 2019.1655646

32. Gharbavi, M.; Johari, B.; Mousazadeh, N.; et al. Hybrid of niosomes and bio-synthesized selenium nanoparticles as a novel approach in drug delivery for cancer treatment. *Mol. Biol. Rep.* **2020**, *47*, 6517–6529. DOI: 10.1007/s11033-020-05683-7

33. Singireddy, A.; Pedireddi, S.R.; Subramanian, S. Optimization of reaction parameters for synthesis of Cyclodextrin nanosponges in controlled nanoscopic size dimensions. *J. Polym. Res.* **2019**, *26*, Art. No: 93. DOI: 10.1007/s10965-019-1743-3